

Efficiency analysis of the cycloidal wave energy convertor under real-time dynamic control using a 3D radiation model

Ali Mohtat, Casey Fagley, Kedar C. Chitale, Stefan G. Siegel

Abstract— Ocean waves provide a vast, uninterrupted resource of renewable energy collocated around large coastal population centres. Clean energy from ocean waves can contribute to the local electrical grid without the need for long term electrical storage, yet due to the current high cost of energy extraction from ocean waves, there is no commercial ocean wave farm in operation. One of the wave energy converter (WEC) device classes that shows the potential to enable economic energy generation from ocean waves is the class of wave terminators. This work investigates the Cycloidal Wave Energy Converter (CycWEC), which is a one-sided, lift-based wave terminator operating with coupled hydrofoils. The energy that the CycWEC extracted from ocean waves was estimated using a control volume analysis model of the 3D wave field in the presence of the CycWEC. The CycWEC was operated under feedback control to extract the maximum amount of energy possible from the incoming waves, and the interaction with different incoming regular, irregular, and short crested waves was examined.

Keywords—Wave energy conversion, Cycloidal wave energy convertor, Deep-water waves, Wave radiation, irregular waves, short crested waves.

I. INTRODUCTION

OCEAN wave energy, if harvested efficiently, has the potential to provide a large portion of world's electric energy needs [4], [5]. Additionally, ocean waves have higher available energy densities, about two and a half times that of solar and more than four times that of wind [4]. The higher energy density, as well as the

predictability of ocean waves, makes them one of the most reliable sources of renewable energy. Unfortunately, with the current state-of-the-art of wave energy convertors (WECs), the cost of wave energy is higher than other renewables. In case of the WECs, there is a direct correlation between cost and efficiency of the device, thus more efficient devices have the potential to produce electrical energy comparable in price to those from other energy sources. A more detailed review of the different types of WECs can be found in McCormick [6], Cruz [7], and Rusu [8].

The most efficient WECs are the ones that are theoretically able to extract all of the energy in the waves. These WECs are known as wave terminators, some of the most well-known being the Salter Duck [9] and the Bristol or Evans Cylinder [10], with floating and fully submerged systems, respectively. Both of these devices operate at the wave induced water velocity with hydraulic power-take-off systems and their main dimension aligned parallel to the wave crests. The low operation velocity of such devices requires large areas to capture large amounts of power, which increases the construction costs and reduces storm survivability. Utilizing hydrofoil lift instead of buoyancy or pressure force can significantly improve the operation velocity of the WEC system. Such lift-based systems can operate at larger velocities than the wave induced particle velocity. Some of the first research on the interaction between hydrofoils and water waves can be found in Wu [11], proving the possibility of a net energy gain. Later, research at TU Delft [12] revealed the ability of rotating wave energy converters to self-synchronize with the incoming waves in terms of rotational phase. With feedback control algorithms to optimize synchronization, the CycWEC was later shown to provide wave termination with better than 99% inviscid efficiency for regular waves [13]. The CycWEC efficiency for irregular waves was found to be between 60% to 80% from numerical and experimental investigations in [14] and [15]. One of the most important observations during the experimental investigation of CycWEC was the presence of 3D radiation effects, the details of which can be found in [16], [17], and [18], along with the sensitivity of the wave cancellation to the offset between the incoming wave phase and rotational angle of the CycWEC shaft.

Manuscript received 27 December, 2021; published 10 June, 2022.

This is an open access article distributed under the terms of the Creative Commons Attribution 4.0 licence (CC BY <http://creativecommons.org/licenses/by/4.0/>). unrestricted use (including commercial), distribution and reproduction is permitted provided that credit is given to the original author(s) of the work, including a URI or hyperlink to the work, this public license and a copyright notice. This work was supported in part by the Department of Energy under grant EE0008626.

This article has been subject to single-blind peer review by a minimum of two reviewers.

A. Mohtat, C. Fagley, K. C. Chitale and S. G. Siegel are at Atargis Energy corporation, 1111 Lavender Way, Pueblo CO 81001 (email: ali.mohtat@atargis.com). Digital Object Identifier <https://doi.org/10.36688/imej.5.45-56>

The CycWEC design considered in this study consists of two hydrofoils connected to a main shaft at a radius, R . The synchronised rotation of the system with the adjusted hydrofoil angles enables the wave cancellation and investigation of radiated wave patterns. A schematic drawing of the CycWEC is presented in Figure 1. The wave cancellation of such a WEC system can be determined by including the 3D radiation effects, similar to those calculated in [4].

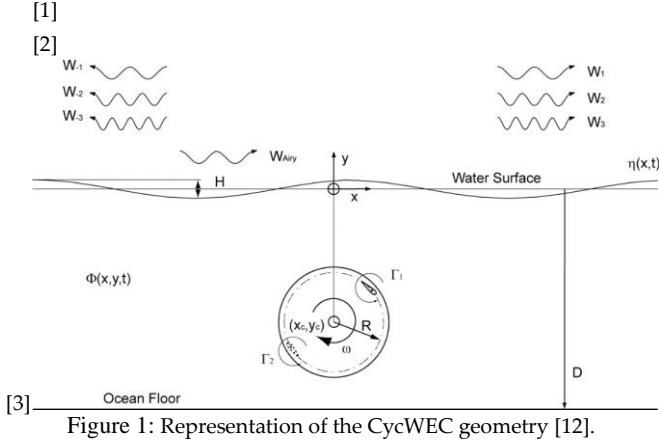


Figure 1: Representation of the CycWEC geometry [12].

First, the radiation wave field of CycWEC system was investigated, then the cancellation wave patterns for different WEC geometries were analysed and finally, the cancellation efficiency of the CycWEC was investigated for regular and irregular waves. To investigate the radiation wave field, the validated 2D wave radiation model, which was based upon potential flow, was extended to a 3D radiation model, which was experimentally validated [19]. Both long crested and directionally-varying short crested sea states were considered for the first time (all previous publications only assumed regular wave radiations). A control volume scheme was used to analyse the cancellation efficiency of the CycWEC by determining the overall energy flux of the combination of the wave environment and the wave interaction of the device.

II. METHODOLOGY AND FORMULATION

A. WEC radiation

To characterize the radiation behaviour of the CycWEC with the incoming wave, a numerical model was required to represent the propagation of the radiated wave field from the source location. The ideal model would be the one which satisfies the conservation of energy exactly and hence, solutions and models involving energy dissipation, such as finite difference-based panel approaches, are not suitable for this type of study. To this end, potential flow theory was adapted to model the radiated wave field caused by a point source. For this formulation, the flow was assumed inviscid, incompressible and irrotational. The governing dynamic equation for potential flow is the Laplace equation,

$$\nabla^2 \Phi = 0 \quad (1)$$

in which Φ is the velocity potential. Unique solutions to the Laplace equations, which satisfied the appropriate boundary conditions based on physical considerations, were derived. Specifically, for the wave radiation model, a kinematic and dynamic boundary condition needed to be satisfied at the free surface. For the kinematic condition, a linearized free surface boundary condition was adapted to represent the free water surface. This was represented by the following relationship,

$$\frac{\partial \eta}{\partial t} - \frac{\partial \Phi}{\partial y} = 0 \quad (2)$$

The dynamic boundary condition was satisfied by ensuring the continuity of pressure on the free surface through Bernoulli's equation. After applying the boundary conditions and solving for the complex potential, the condition was given by,

$$F(z, t) = \frac{\Gamma(t)}{2\pi i} \ln \left(\frac{z - c(t)}{z - \bar{c}(t)} \right) + \frac{g}{\pi i} \int_0^t \int_0^\infty \frac{\Gamma(\tau)}{\sqrt{gk}} e^{-ik(z - \bar{c}(\tau))} \sin(\sqrt{gk}(t - \tau)) dk d\tau \quad (3)$$

which essentially captured the radiation at point z on a free surface due to a motion $c(t)$ of a point vortex $\Gamma(t)$. From the complex potential, the surface elevation could be computed through the kinematic boundary condition, or the velocity potential that was taken from the real part of the complex potential,

$$\Phi_{2D} = \Re(F(z, t)) \quad (4)$$

This formulation is 2D in nature, and while an extension to 3D can be shown through the use of quaternions or hypercomplex spaces, those formulations are beyond the scope of this paper. The previous experimental observations in a 1:10 scale wave tank test showed a unique spreading or radiation behaviour [20], thus, a 3D model could be employed based on those observations. The proposed model incorporates a radial wave height reduction and azimuthal modulation of the form,

$$\Phi_{Wec}(r, \theta) = \frac{\Phi_{2D}}{2\sqrt{r}} (\cos(2\theta) + 1) \quad (5)$$

where θ is the azimuthal angle from the source location and r , the radial distance. As stated, the 3D behaviour directly corroborated experimental measurements in a 1:10 scale wave tank test.

In order to conserve energy, a panel approach, which solved the wave equation with a finite difference scheme, would not be useful for this study, as energy dissipation would violate the conservation of energy and not suitably represent the radiation gains/losses

In addition to the 3D propagation behaviour of the 2D radiation potential, the hydrofoil was modelled as a finite span (s) hydrofoil with an elliptic distribution as shown

in Figure 2. The finite span was discretized by point vortices with an elliptical circulation distribution shown in Figure 2.

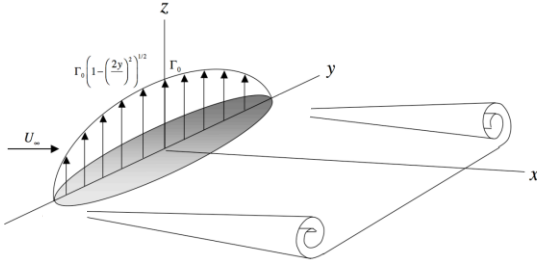


Figure 2: Elliptic lift distribution across hydrofoil span, after [6].

B. Environmental (wave) modelling

The environmental condition (wave field) for the 3D radiation model was assumed to represent a real-life wave environment containing temporal, spatial, and directional variation. The standard accepted approaches, based on regular linear waves, found in [7,8] were used. Specifically, the irregular incident field was modelled using a linear superposition of a finite number of linear regular wave components. The fidelity of the irregular wave field increased as the number of wave components was increased. According to [9], a minimum of 20 wave components are required for modeling a unidirectional irregular sea state. The amplitude for component i was based on a specified wave spectrum according to

$$a_{ij} = \frac{H_i}{2} = \sqrt{2S_I(\omega_{ij})D(\omega_{ij}, \theta_{ij})\Delta\omega\Delta\theta} \quad (6)$$

where S_I is the spectral density and $\Delta\omega$, the wave frequency interval for component i . For the presented study, the incident wave field was modelled using the Bretschneider wave spectrum. The Bretschneider spectrum is a commonly used two parameter model for wave spectra in the open ocean and is defined as [8],

$$S_I(\omega) = \frac{48H_s^2}{T_s^4\omega^5} e^{-\frac{1948}{T_s^4}\omega^4} \quad (7)$$

where H_s is the significant wave height and T_s , the significant wave period associated with the peak energy. For the purposes of this paper, the standard wave conditions were given by a significant wave period of 8 seconds with a significant wave height of 1 meter, but the results can very easily be scaled to different wave environments. Additionally, the Bretschneider spectrum was discretized by a total of 30 components in a range of $0.5T_s$ to $1.5T_s$, and the individual phases of the wave components were randomly selected in the interval of $[0, 2\pi]$.

To model the directionally spreading ($D(\omega_i, \theta_i)$) of a short-crested wave environment, a common form of directional spreading was incorporated, which used the frequency dependent cosine power function which is found in [8]. The equation for the directional spreading is

$$D(\omega, \theta) = \frac{\Gamma(si + 1)}{\Gamma\left(si + \frac{1}{2}\right)\pi} \cos^{2s}(\theta - \theta_0) \quad (8)$$

$$\theta \in \left[-\frac{\pi}{2}, \frac{\pi}{2}\right]$$

where si is the spreading index and θ_0 represents the principal wave travel direction. A similar number of components were chosen to discretize the directional vector and superimposed with a random phase. As the spreading index became larger, the directionality of the associated wave heights became narrower, and as the index increased toward infinity, the long crested irregular wave was recovered.

C. 3D Wave radiation control volume

To determine the overall efficiency of the CycWEC, a control volume analysis was used to compute the energy flux through a boundary far from the point source. To accurately compute the energy transport caused by the kinetic motion of particles of the fluid and the potential energy of the induced fluid height, the velocity potential (Φ) was required along an enclosed volume (Ω). The velocity potential of regular linear wave components (Φ_w) was superimposed with each of the vortex potential wave components (Φ_{wec}) of the CycWEC model along the boundary to form the total velocity potential (Φ_T) which was written as,

$$\Phi_T(x, z, t) = \Phi_w(x, z, t) + \sum_{i=1}^N \Phi_{c_i}(x, z, t) \quad (9)$$

For infinitely deep water, the velocity potential of a linear regular wave is

$$\Phi = \Re e \left\{ \frac{iH_w g}{2\omega} e^{(kz + ikx - i\omega t + \varphi)} \right\} \quad (10)$$

where z is the coordinate in the vertical or depth direction, and φ represents the initial phase. The energy at any instant in the flow is given by the sum of the potential and kinetic energy, which can be written as,

$$E(t) = \frac{1}{2} \rho v^2 + gy \quad (11)$$

The overall energy flux, $P(t)$, is equivalent to the rate of change of the energy density, $dE(t)/dt$, and from potential flow theory could be shown to be,

$$P(t) = \frac{dE(t)}{dt} = \rho \iiint_{\Omega} \frac{\partial}{\partial t} \left(\frac{1}{2} \rho v^2 + gy \right) d\Omega \quad (12)$$

$$= \rho \iiint_{\Omega} \nabla \cdot \left(\frac{\partial \Phi_T}{\partial t} \nabla \Phi_T \right) d\Omega$$

invoking Gauss's theorem which equates the divergence of a vector field within a closed volume to the flux of a vector field through a closed surface. The equation for the energy flux can be written as,

$$P(t) = \iint_{\xi} \frac{\partial \Phi_T}{\partial t} \nabla \Phi_T \cdot \vec{n} d\xi \quad (13)$$

where \vec{n} was the normal vector to the surface defined by ξ with area $d\xi$. For simplicity, a rectangular, cartesian

control volume was employed at varying distances from the point sources and extended to infinitely large depths. The equation above was solved for each side of the control volume and simplified to

$$P(t) = \int_{-\infty}^0 \frac{\partial \Phi_T}{\partial t} \frac{\partial \Phi_T}{\partial n} dy \quad (14)$$

for flux across a vertical fluid boundary. The control volume numerical scheme was verified and validated against individual wave components, i.e., the power in the linear regular wave, $P_w = 1/8 \rho g H_w^2 C_g$, which was exactly equal to the result of the control volume analysis. In addition, convergence metrics were determined for that of a point source superimposed with a plane wave (i.e., representing the radiation patterns of a circular point absorber) and extended to subsequent wave generator models. The validation and verification of the control volume scheme can be found in [15].

Upon computing the net energy flux through the domain, the capture width length C_w could be defined as the ratio of the extracted power to the power per meter of wave crest of incoming wave times the wavelength.

$$CW = \frac{P(t)}{1/8 \rho g H_w^2 C_g} \quad (15)$$

where the net power through the control volume was normalized by the power per unit meter of wave crest of the incoming wave for a regular wave. The power for the directionally varying irregular sea state was defined by the sum of each of the individual wave components. This metric indicated a length at which the device was effective at capturing the power in the incoming wave and could be compared with the device size, the span. For a perfect terminator, the capture width would be exactly equal to the device size. Finally, the capture width length in which the capture width ratio was normalized by the span gave a good reference of power capture capabilities of different device scales.

III. RESULTS AND ANALYSIS

The radiated waves from the CycWEC were generated for different normalized hydrofoil spans (s/λ , with λ presenting the wavelength) using both regular and irregular wave conditions. The frequency and amplitude of the source terms were defined using the assumed incoming wave characteristics. For example, under regular wave conditions, only one amplitude and frequency were adapted and for irregular waves, the amplitudes and frequencies were matched with each individual wave component. In general, the incoming waves were traveling left to right in the positive x direction, and the span of the CycWEC was represented by a dark-grey rectangle.

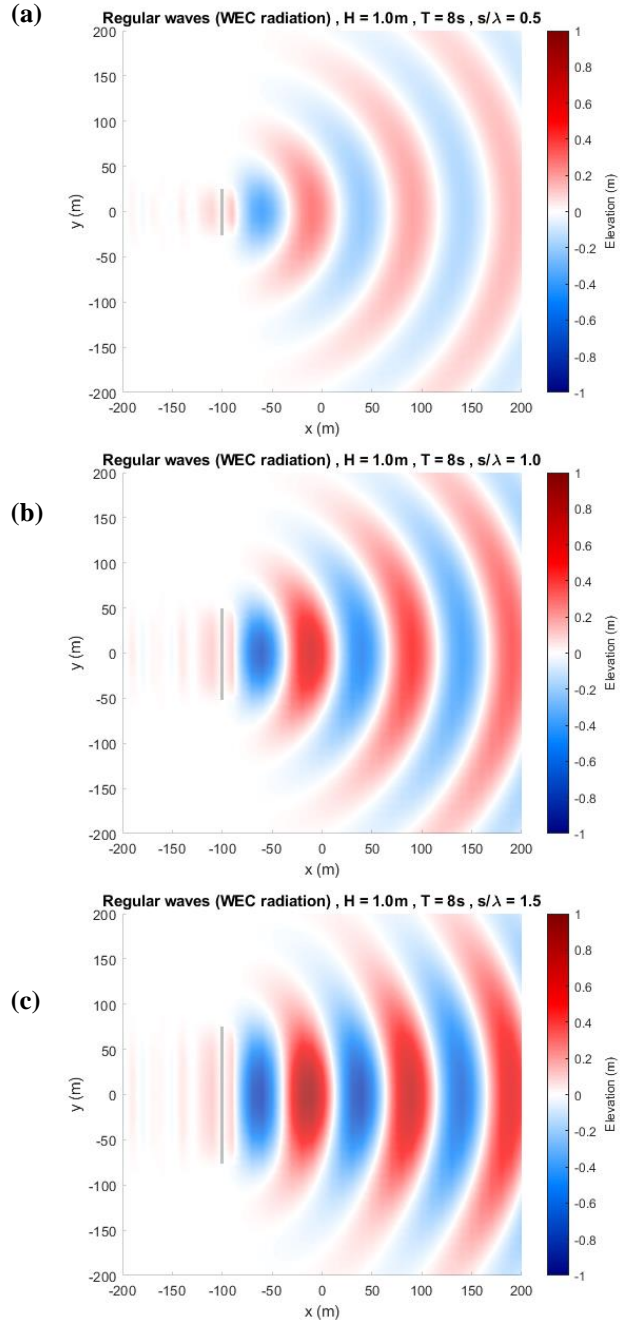


Figure 3: The instantaneous surface elevation for a regular wave for different WEC spans, (a) $s/\lambda = 0.5$, (b) $s/\lambda = 1.0$, and (c) $s/\lambda = 1.5$.

The surface elevations of the radiated wave field from the CycWEC, with regular wave generation are presented in Figure 3 for different span ratios of $s/\lambda = 0.5, 1.0$, and 1.5 in (a), (b), and (c), respectively. The constant spacing between the red and blue contours shows the constant period of the radiated waves under the regular generation of CycWEC. Using the same colour bar limits for all figures shows an increase in amplitude of the radiated wave field with increasing span to wavelength ratio, amplitudes of about 0.5m , 0.7m , and 0.85m for $s/\lambda = 0.5, 1.0$, and 1.5 , respectively. Comparing Figure 3(a)-(c) reveals the increase of amplitude of the radiated wave field, specially at the centre of the WEC, with increasing span ratio. Also, a weak wave field formation can be observed upstream of the WEC location, which

although not visible in the plots, is a standing wave representing the evanescent mode that does not radiate. Finally, as the span ratio increases, a straighter region can be observed in the vicinity of the WEC centre.

To better understand the behaviour of the radiated wave field, Figure 4 shows the averaged wave height of the radiated waves from the CycWEC for the same span ratios as the wave fields shown in Figure 3, of $s/\lambda = 0.5, 1.0$, and 1.5 in (a), (b), and (c), respectively. It can be observed from Figure 4(a) to (c) that with increase in span ratio, the extent of the radiated wave field increases in the spanwise direction, which is an important indication of the scalability of the CycWEC system: A larger radiated wave field can interact with a larger amount of incoming wave power. Also, an interesting observation is a decrease in the area that the radiated waves were spreading (represented by dashed black lines in the figures as spreading angle), down wave from the CycWEC, with the increase in span ratio. This behaviour is similar to the experimental observation presented in [24]. Figure 3 and Figure 4 clearly show the generated wave field down wave of the WEC location. With correct phase relative to an incoming wave, this wave field could cancel the incoming waves and extract most of the energy of an incoming wave, as will be shown later.

The same procedure was conducted with irregular waves, following a Bretschneider wave spectrum. The amplitude and initial phase of the CycWEC blades are adjusted with the significant wave height and period of the generated wave train by CycWEC, and the shaft rotation was synchronized with each individual wave that passed by the WEC. The free surface elevation of the radiated wave field is presented in Figure 5(a)-(c) for different span ratios of $s/\lambda = 0.5, 1.0$, and 1.5 in (a), (b), and (c), respectively. Different frequencies of the generated individual waves can be observed by the varying spacing of the colour bars, representing the wavelength. Similar to Figure 3, with increasing span ratio, the amplitude of the radiated wave field increases. This increase, both in regular and irregular wave generation, can be attributed to the control scheme which enforces the amplitudes of the generated waves, to the assumed values, at tips of the CycWEC defining the phase shift between the incoming waves and shaft. This amplitude control, along with distribution function defined for 3D source term (equation for Φ_{Wec}) results in some regions with larger (and smaller) wave heights, in comparison to the target. More details on the control algorithm can be found in [25]. The observed spatial distribution of the significant wave height of the radiated wave field for irregular waves, presented in Figure 6, is similar to that generated under the regular wave condition, with a decreasing spreading angle of the generated wave field as the span to wavelength ratio increases. In the next section we present the interactions between the radiated and incoming wave, which with appropriate phase matching of the CycWEC shaft angle

to the incoming waves, results in the cancellation of the incoming waves.

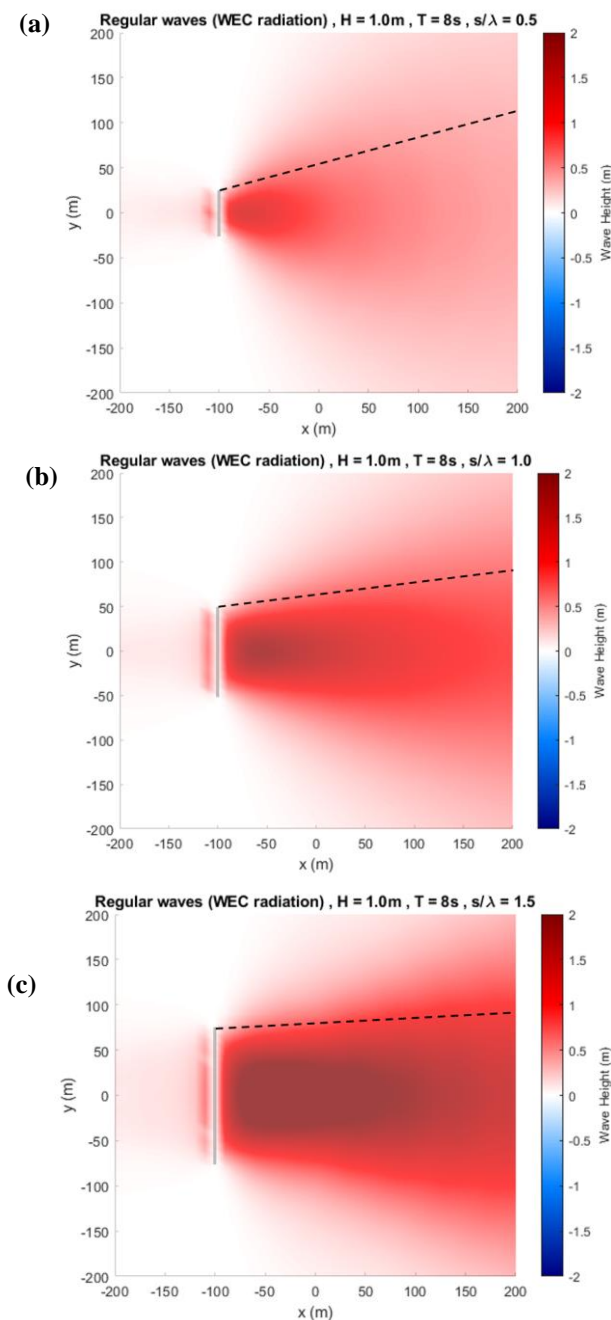


Figure 4: The time averaged wave height of the radiated wave field for a regular wave for different WEC spans, (a) $s/\lambda = 0.5$, (b) $s/\lambda = 1.0$, and (c) $s/\lambda = 1.5$. The dashed line represents the spreading angle.

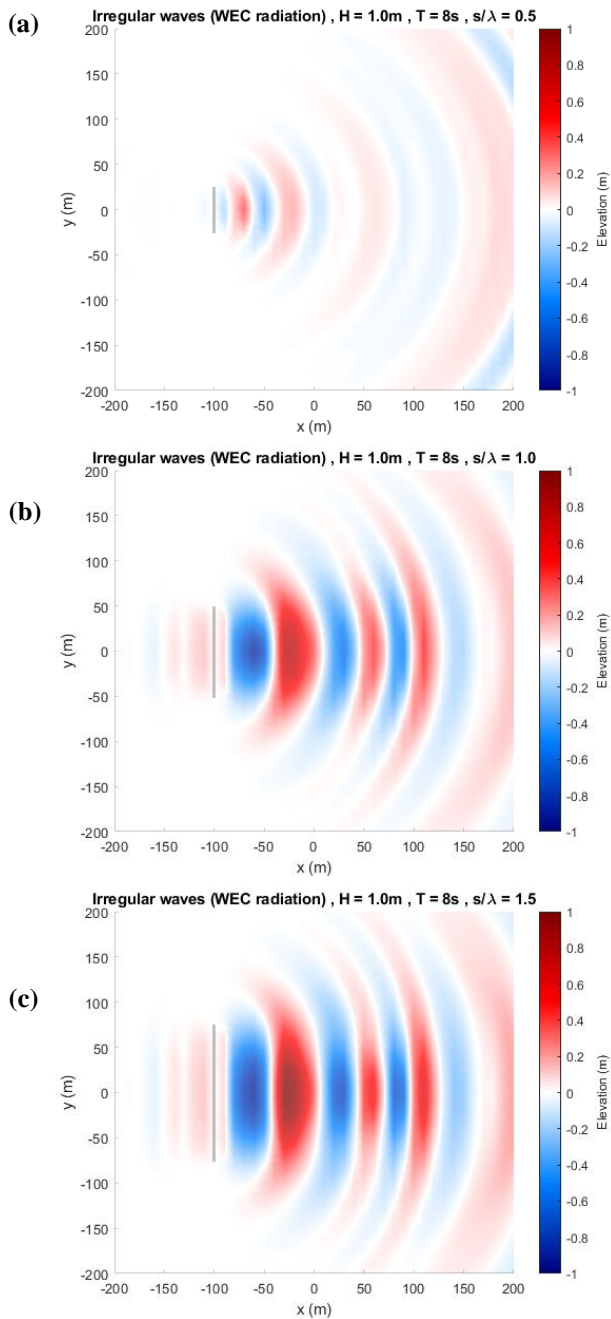


Figure 5: Instantaneous snapshot of the radiated wave field for an irregular wave for different WEC spans, (a) $s/\lambda = 0.5$, (b) $s/\lambda = 1.0$, and (c) $s/\lambda = 1.5$.

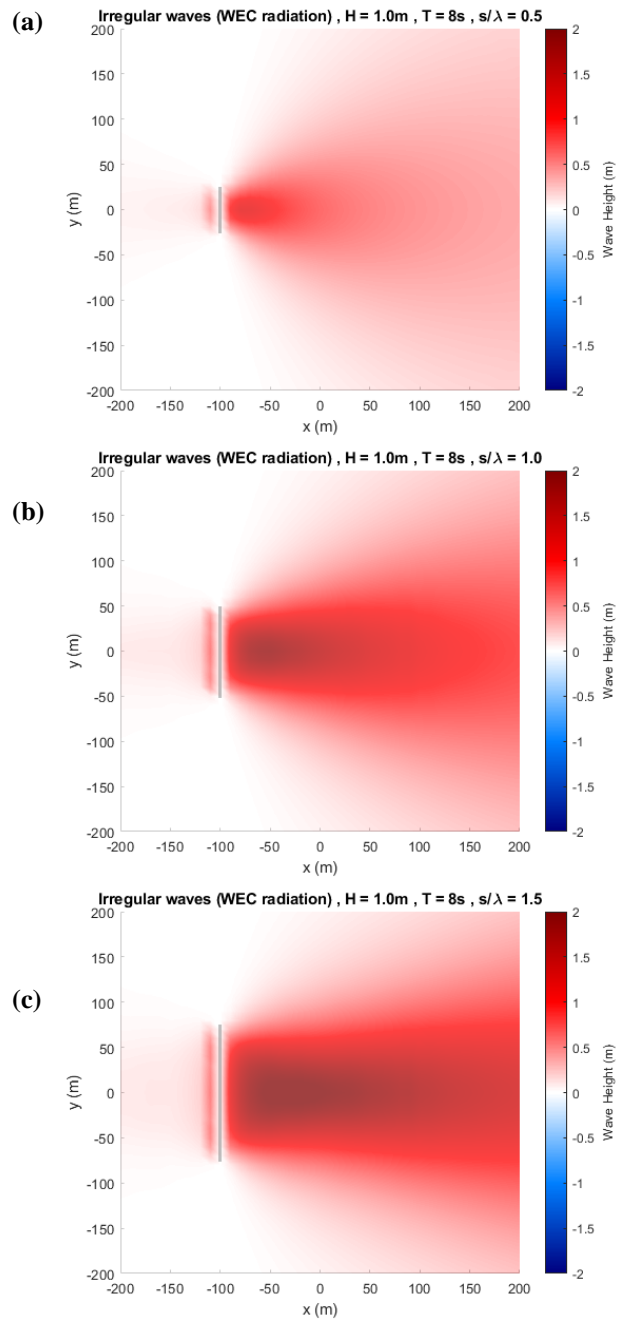


Figure 6: The time averaged significant wave height of the radiated wave field assuming an irregular wave condition for different spans, (a) $s/\lambda = 0.5$, (b) $s/\lambda = 1.0$, and (c) $s/\lambda = 1.5$

IV. WAVE CANCELLATION

The resulting wave field in presence of the CycWEC can be constructed from the interaction (superposition) of the incoming waves with the waves radiated from the WEC shown in the previous section. To investigate the cancelation behaviour of the CycWEC, different span ratios, with regular and irregular incoming waves were simulated and results are presented in terms of the difference between the final wave field and the incoming waves (significant wave height for irregular waves). In this analysis, negative values represent the energy extracted by the WEC from the incoming waves.

An example of the free surface elevation of the WEC interacting with incoming regular waves with $s/\lambda = 0.5$ is presented in Figure 7. This figure shows the formation of larger and smaller wave regions down wave of the WEC, presented in a lighter red colour (for crests) and blue (for troughs), which can be hard to see and follow. Hence, to better examine the resulting wave field under the regular wave condition, the superimposed time averaged wave fields, of the incoming and radiated waves, are presented in Figure 8(a)-(c) for different span ratios of $s/\lambda = 0.5, 1.0$, and 1.5 in (a), (b), and (c), respectively. The blue region represents the area where the resulting wave height is smaller than the incoming wave, which shows a reduction in height of waves due to the interaction of the radiated wave field with the incoming waves. The reduction wave height regions (coloured blue) in these figures are similar to the radiated wave heights shown in Figure 4 due to the simple superposition of the incoming waves with the radiated ones. The superposition of the radiated waves from the CycWEC with the incoming waves resulted in a low energy region, hereafter referred to as the wake region, down wave from the WEC. Similarly, with increasing span ratio, (a) to (c) in, the spreading angle of the wake region decreases. Also, there is an increase in resulting wave height outside of the wake region (shown in red), which decreases the energy extraction efficiency since the power for this increase in wave height needs to be supplied by the WEC. These two effects together (wake minus losses due to increased wave height) represent the net energy extracted by the WEC.

Defining the initial location (shaft angle) of the hydrofoils enables the control of the generated (radiated) waves from the WEC and their exact location. For example, in all the cases presented in this paper, the target wave heights are generated close to the tips of WEC. Hence, for larger span ratios in Figure 8(b) and (c) a bump (a region with larger wave heights) is visible in the wake region close to the WEC centre. This increase in wave height also represents a power loss since the increase in wave height needs to be supplied by the WEC. This shows the importance of phase shift (between the incoming waves and shaft angle) in optimization of the energy-take-off under different WEC geometry and wave conditions.

The superimposed wave field shows a similar behaviour with the radiation patterns with respect to the spreading angle of the wake region decreasing with increasing s/λ . Due to the fact that the phase shift of the CycWEC hydrofoil was kept constant during the simulations, a central bump (a region with larger wave height relative to the incoming waves) can be seen. This is due to the fact that with the chosen phase shift the incoming wave phase is matched at the tips of the hydrofoils of the CycWEC and not at the centre. Here it can be observed that the plane Airy wave, which is superimposed with the irradiance of the rotating vortex model, is reduced in height just beyond the CycWEC, creating a wake region. Additionally, this wake region extends beyond the span which accounts for the radiative gains and results in a capture width larger than the device span. In comparison, Figure 7(c) shows a larger span CycWEC which demonstrates more two-dimensional cancellation and a reduction of radiative gains.

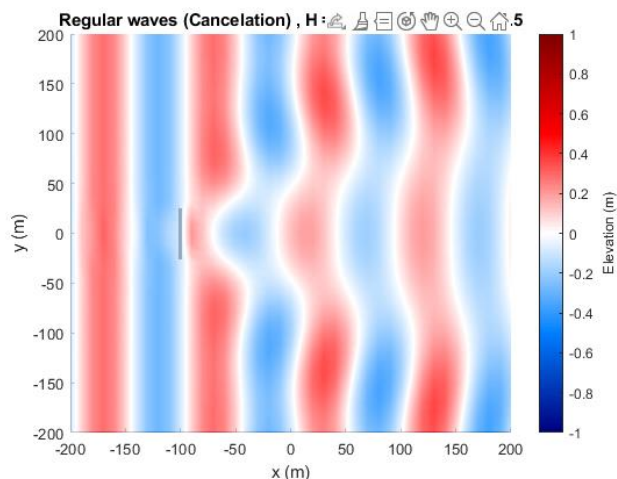


Figure 7: The resulting free surface elevation under regular wave condition with $s/\lambda = 0.5$.

The same procedure was conducted for irregular waves and a snapshot of the free surface elevation of the resulting wave field under incoming irregular waves is presented in Figure 9. In this figure, similar to the regular waves, modulations along the waves can be observed down wave from the WEC. Again, for further understanding of the interaction, the resulting average wave height is presented in Figure 10(a)-(c) for different span ratios of $s/\lambda = 0.5, 1.0$, and 1.5 in (a), (b), and (c), respectively. Similar behaviour with respect to regular waves is observed.

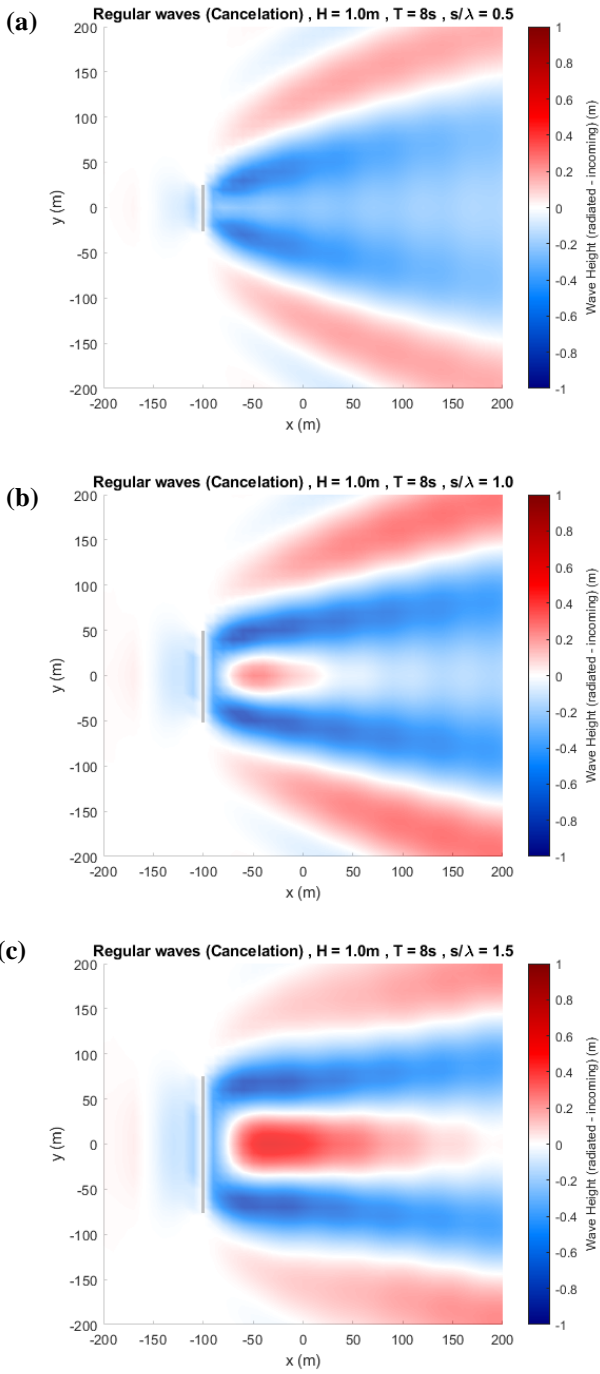


Figure 8: The wave height of the resulting (cancellation) wave field assuming regular wave condition for different spans, (a) $s/\lambda = 0.5$, (b) $s/\lambda = 1.0$, and (c) $s/\lambda = 1.5$.

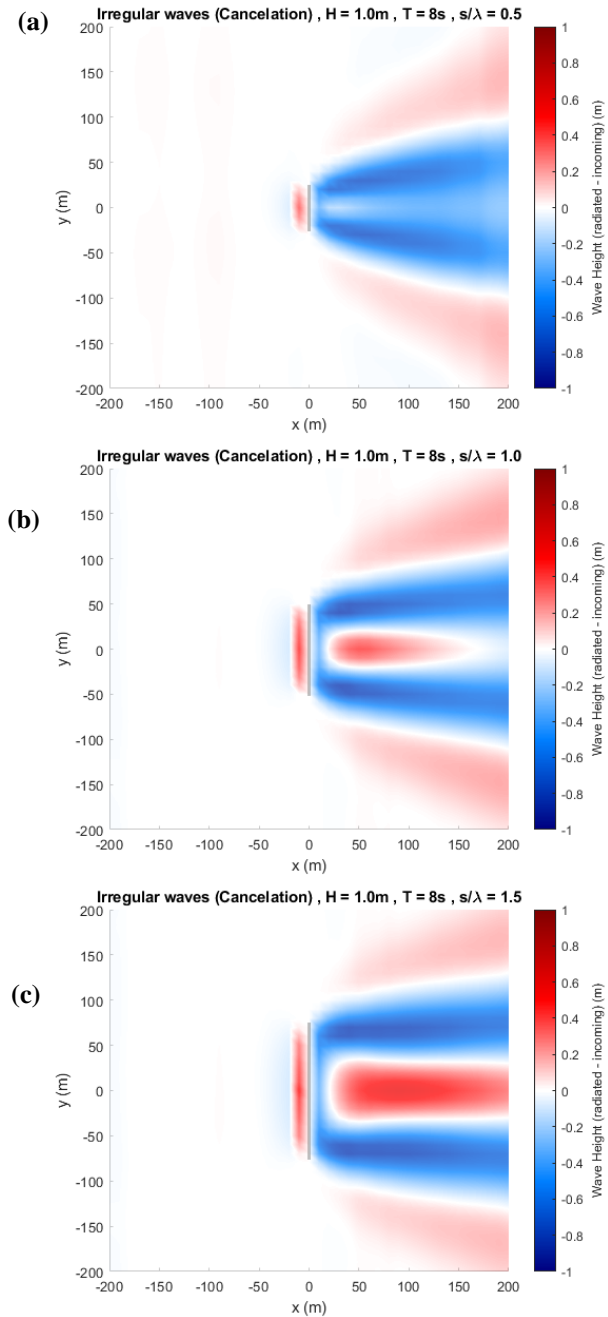


Figure 10: The significant wave height of the resulting (cancellation) wave field assuming irregular wave condition for different spans, (a) $s/\lambda = 0.5$, (b) $s/\lambda = 1.0$, and (c) $s/\lambda = 1.5$

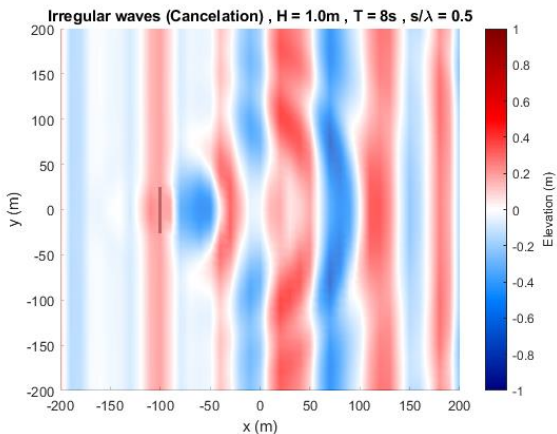


Figure 9: The radiated wave elevation assuming irregular wave condition $s/\lambda = 0.5$.

One of the main concerns of the WEC operators is the performance of the WEC under short-crested waves. The short-crested waves can be simulated defining the spreading index (si) in the directional spreading spectrum definition. Different spreading indices of 15, 35, and 55, were used in the short-crested wave simulations and the resulting wave patterns were investigated and presented in this section. The free surface elevation results are presented in Figure 11(a)-(c) for a constant span ratio of $s/\lambda = 0.5$ and different spreading indexes of $si = 15, 35$, and 55 in (a), (b), and (c), respectively. It can be seen from Figure 11 that, with increasing values of the spreading index (from 15 to 55 in figures (a) to (c)) the short-crested wave fields start approaching a long-crested wave field. To analyse the interaction between the WEC

and the incoming wave, the time averaged significant wave height of the resulting wave field is presented in Figure 12(a)-(c) for a constant span ratio of $s/\lambda = 0.5$ and different spreading indices of $si = 15, 35$, and 55 in (a), (b), and (c), respectively. It is clear that by increasing si values, the wake region upstream of the CycWEC becomes stronger and clearer, by comparing the shade of blue in the wake region turning to a darker blue with increasing si . The fact that the presented CycWEC system can extract energy even in very short-crested wave fields extends the operational wave conditions of the WEC.

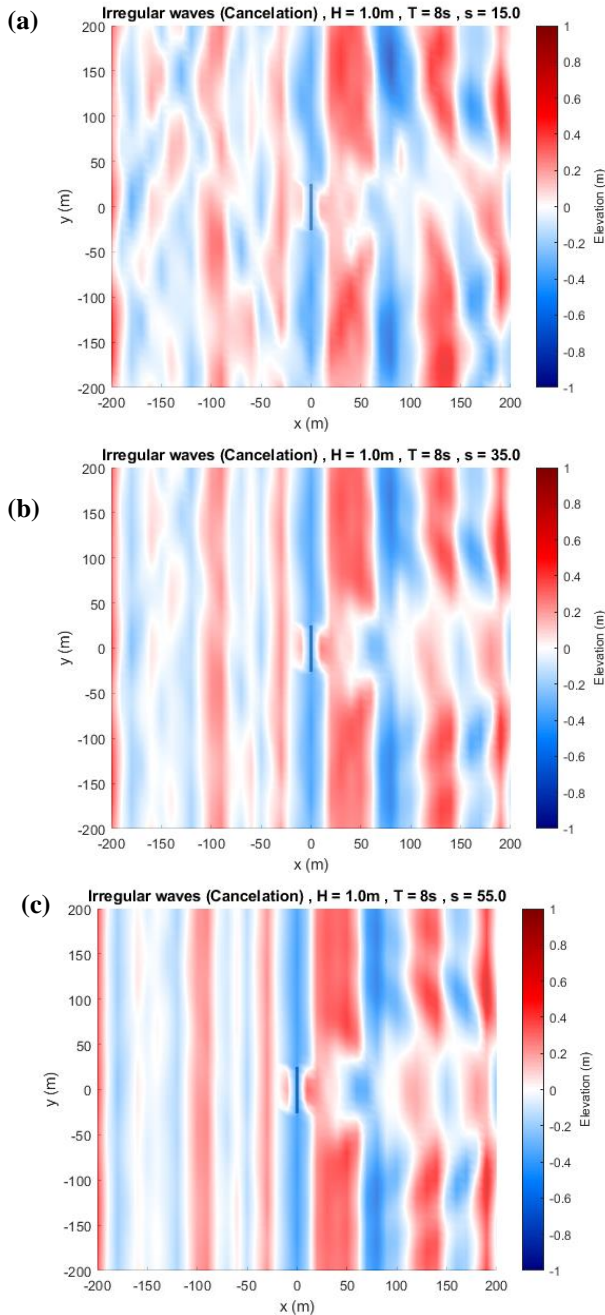


Figure 11: The instantaneous free surface elevation of the wave field for short crested wave conditions for different spreading indexes of, (a) $si = 15$, (b) $si = 35$, and (c) $si = 55$ with $s/\lambda = 0.5$.

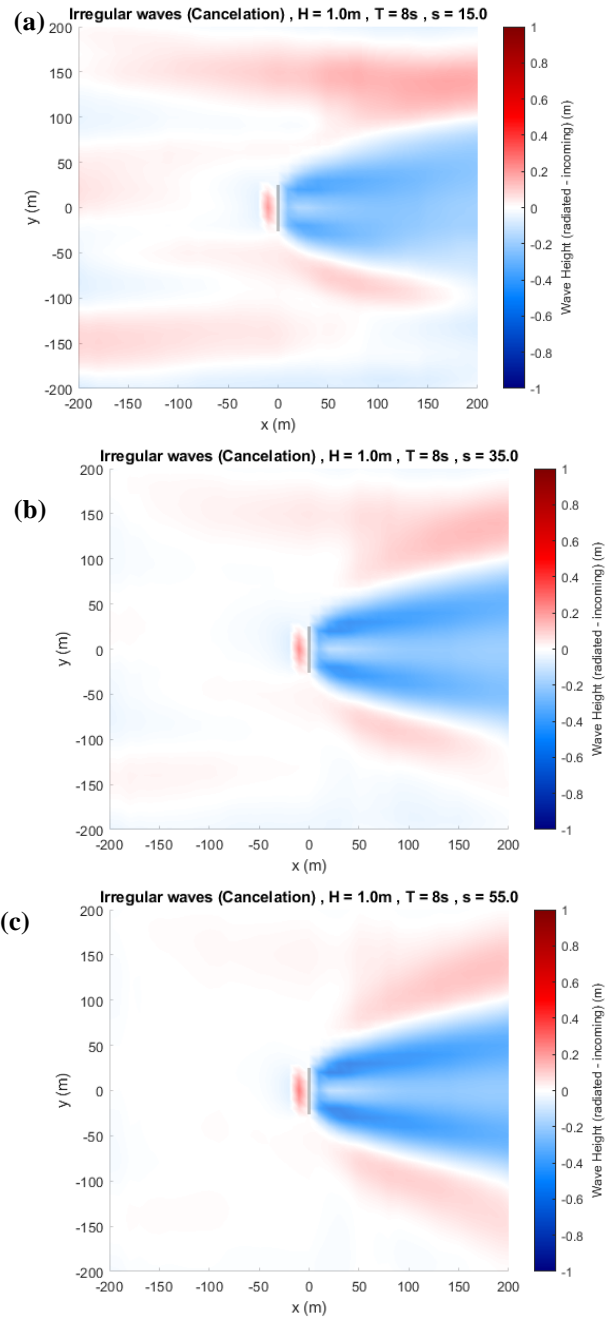


Figure 12: The significant wave height of time averaged wave field for short crested wave conditions for different spreading indexes of, (a) $si = 15$, (b) $si = 35$, and (c) $si = 55$ with $s/\lambda = 0.5$.

V. EFFICIENCY ANALYSIS OF THE CYCWEC

The following sections show the CycWEC performance for Airy wave cancellation, irregular wave cancellation and, finally, a directionally spread irregular wave. For these runs, the CycWEC was controlled by a predetermined wave phase and amplitude to not incur losses introduced from the wave estimator. The efficiency of the CycWEC was examined using the capture width concept though control volume analysis of the domain.

Initially, the resulting wave field for incoming regular waves were examined for different span ratios. The resulting time-averaged wave heights are presented in Figure 13(a)-(c) for different span ratios of $s/\lambda = 0.5, 1.0$, and 1.5 in (a), (b), and (c), respectively. The capture width

(C_w) for each case is plotted as a green solid line. It can be seen from these figures that for a small span ratio ($s/\lambda = 0.5$) in Figure 13(a), the $C_w/s = 1.6$, which shows that CycWEC was able to extract energy in a width larger than its original span, through the 3D radiation phenomenon. As the span ratios increase, the C_w/s converges closer to 1 as it was found to be 1.2 and 1.0 for $s/\lambda = 1.0$ and 1.5. These results agree with those found by [26] proving the scalability of energy extraction of the CycWEC with respect to span: The extracted power increases approximately proportional with span.

The same procedure was conducted for irregular waves and the resulting significant wave heights are presented in Figure 14(a)-(c) for different span ratios of $s/\lambda = 0.5, 1.0$, and 1.5 in (a), (b), and (c), respectively. The capture width (C_w) for each case is plotted as a solid green line. It was expected that a similar behaviour in energy extraction, through capture width, would be observed for irregular waves as well. Although similar reduction in C_w/s for increasing span ratios was observed, the overall values were smaller than those for regular waves. For irregular waves, C_w/s was found to be 1.0, 0.8, and 0.78 for $s/\lambda = 0.5, 1.0$, and 1.5 , respectively.

Finally, the performance of CycWEC was examined in a directionally spreading irregular wave field under spreading indices of 15, 35, and 55. The resulting significant wave heights are presented in Figure 15(a)-(c) for a constant span ration of $s/\lambda = 0.5$ and different spreading indices of $si = 15, 35$, and 55 in (a), (b), and (c), respectively. Similar results to Figure 12 were observed and with increasing spreading index, capture width increased and converged to those found for the long-crested irregular waves. For directionally spread irregular waves, C_w/s was found to be 0.5, 0.84, and 1 for $si = 15, 35$, and 55 , respectively. These results show the scalability of the CycWEC power extraction with larger spans even for very short-crested wave conditions.

VI. CONCLUSION

The efficiency of a cycloidal wave energy convertor (CycWEC) was examined using numerical 3D wave radiation simulations. Wave fields generated by the CycWEC motion alone were analysed for different span ratios under regular and irregular wave conditions. It was concluded that for both regular and irregular waves, an increase in span ratio results in a reduction in the spreading angle of the radiated wave field down wave from the CycWEC. Also, the phase shift between the incoming wave and shaft angle was found to be of high importance in optimizing the performance of the WEC.

An examination of the resulting wave field and the superposition of the incoming waves with radiated waves, was conducted and a low energy wake region down wave from the WEC was observed. This wake region represents the energy extracted from the incoming waves by the CycWEC. Different directionally spread irregular wave fields, with different spreading indices,

were simulated and results indicated that even under very short crested wave conditions, CycWEC is still able to extract energy from the incoming wave field.

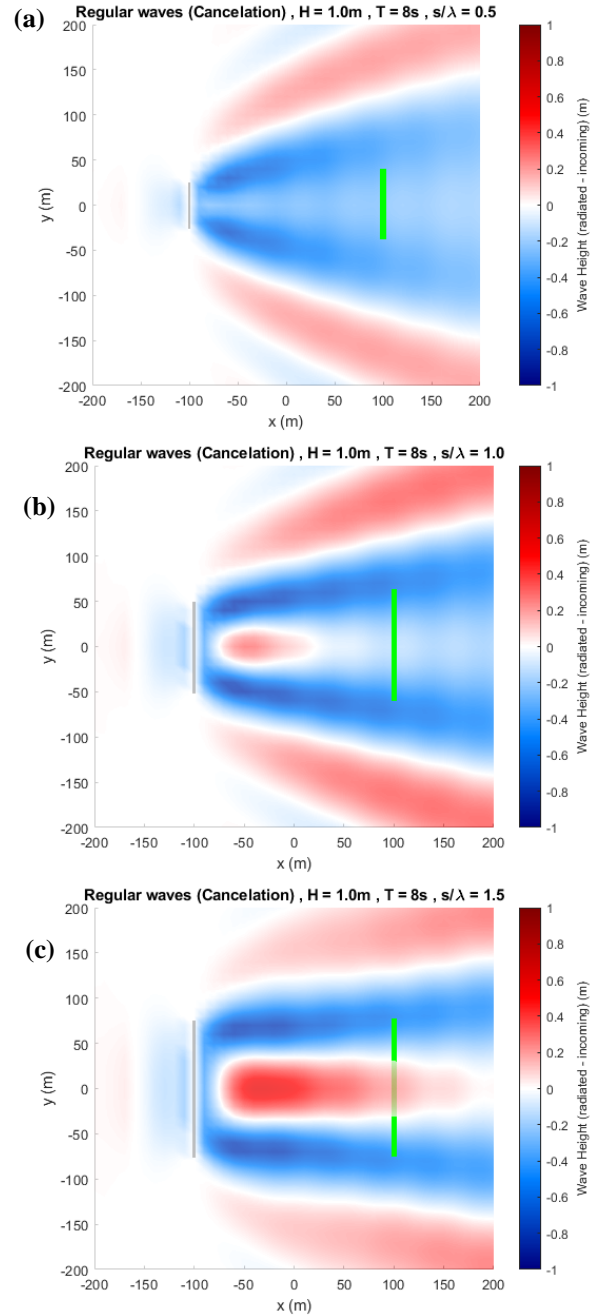


Figure 13: The wave height of the resulting (cancellation) wave field assuming regular wave condition for different spans, (a) $s/\lambda = 0.5$ and (b) $s/\lambda = 1.0$. Green solid line represents the capture width.

Finally, using control volume analysis, the efficiency of the CycWEC was analysed under different wave conditions (regular, irregular, and short-crested). The capture width length, an indication of energy extraction of the WEC system, showed that for regular waves with a small span ratio, the energy extraction length is larger than the span itself. As span ratio increase, the capture width converges toward the span which proves the scalability of energy extraction of the CycWEC with span. The same results were observed for irregular waves

although the computed capture widths were lower than those found for the regular waves. This may be due to the sensitivity of the energy extraction to the defined phase shift between the incoming waves and shaft angle, and may thus be improved in the future with an optimized control approach. For directionally spread irregular waves, the capture width found to be half of the span for the largest spreading index, and it increased toward one (corresponding to the long-crested irregular wave value under similar span ratio) as spreading index increased. Readers are encouraged to read a detailed study on the efficiency of the CycWEC in [27].

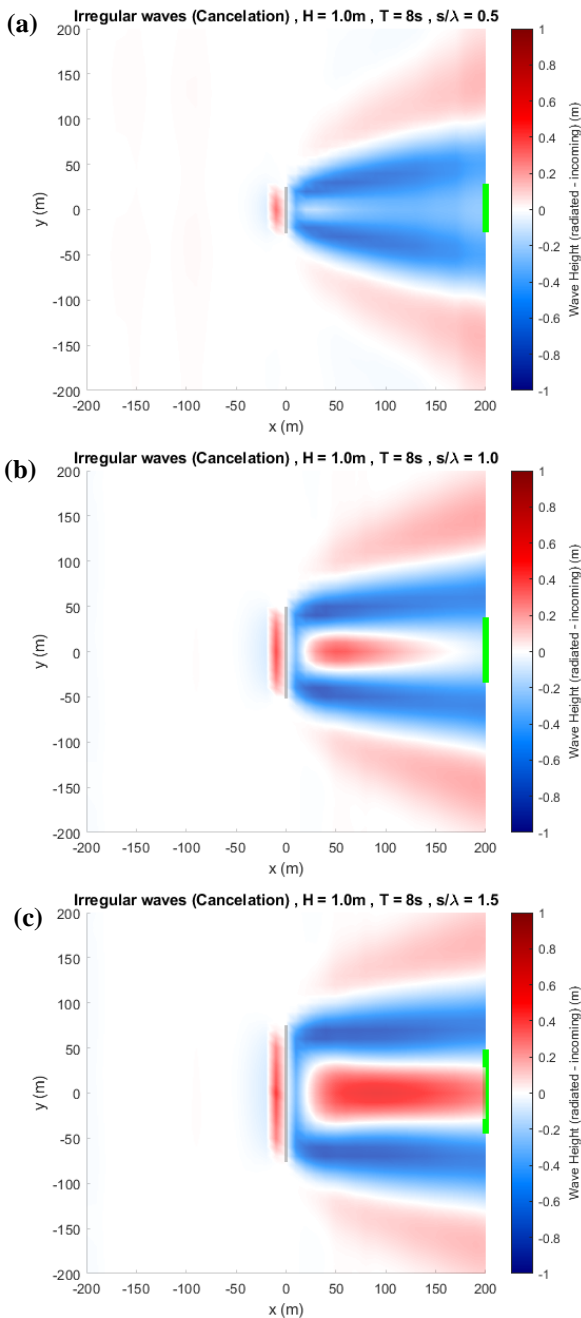


Figure 14: The significant wave height of the resulting (cancellation) wave field assuming irregular wave condition for different spans, (a) $s/\lambda = 0.5$, (b) $s/\lambda = 1.0$, and (c) $s/\lambda = 1.5$. Green solid line represented the capture width.

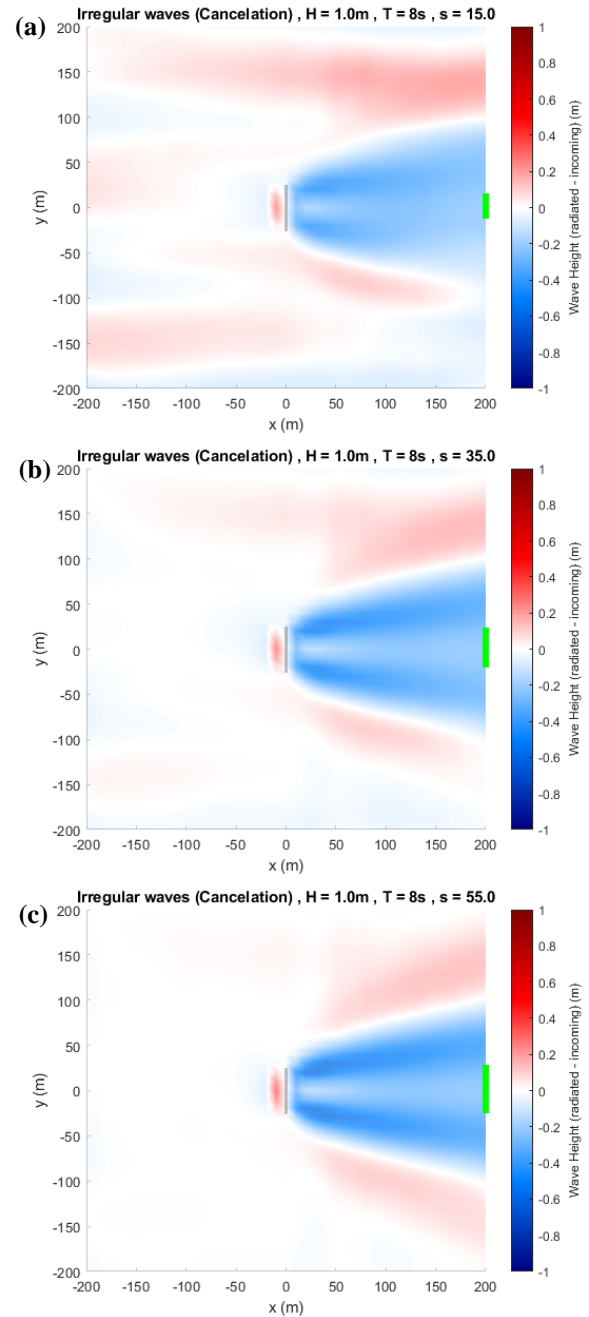


Figure 15: The significant wave height of time averaged wave field for short crested wave conditions for different spreading indexes of, (a) $si = 15$, (b) $si = 35$, and (c) $si = 35$ with $s/\lambda = 0.5$. Green solid line represents the capture width.

VII. DISCLAIMER

This report was in part prepared as an account of work sponsored by an agency of the United States Government. Neither the United States Government nor any agency thereof, nor any of their employees, makes any warranty, express or implied, or assumes any legal liability or responsibility for the accuracy, completeness, or usefulness of any information, apparatus, product, or process disclosed, or represents that its use would not infringe privately owned rights. Reference herein to any specific commercial product, process, or service by trade name, trademark, manufacturer, or otherwise does not necessarily constitute or imply its endorsement, recommendation, or favouring by the United States

Government or any agency thereof. The views and opinions of the author expressed herein do not necessarily state or reflect those of the United States Government or any agency thereof.

VIII. ACKNOWLEDGMENTS

The authors would like to thank Ms. Freia Siegel for proofreading the paper. This material is partially based upon work supported by the Department of Energy under Award Number DE-EE0008626.

REFERENCES

- [4] S. G. Siegel, "Wave radiation of a cycloidal wave energy converter," *Applied Ocean Research*, vol. 49, pp. 9-19, 2015.
- [5] G. Boyle, "Renewable energy: power for a sustainable future," Vol. 2. Oxford University Press, 1996.
- [6] M. McCormick, *Ocean Wave Energy Conversion*, John Wiley & Sons, 1981.
- [7] J. Cruz, *Ocean wave energy: current status and future perspectives*, Springer-Verlag, 2008.
- [8] E. Rusu and F. Onea, "A review of the technologies for wave energy extraction," *Clean Energy*, vol. 2, no. 1, pp. 10-19, 2018.
- [9] SH. Salter, "World progress in wave energy-1988," *Int J Amb Energy*, vol. 10(1), pp. 3-24, 1989.
- [10] D. V. Evans, D. C. Jeffrey, S. H. Salter, and J. R. M. Taylor, "Submerged cylinder wave energy device: theory and experiment," *Applied Ocean Research*, vol. 1(1), pp. 3-12, 1979.
- [11] T. Y.-T. Wu, "Swimming of a waving plate," *Journal of Fluid Mechanics*, vol. 10, pp. 321-344, 1961.
- [12] C. Marburg, "Investigation on a Rotating Foil for Wave Energy Conversion," 1994.
- [13] S. G. Siegel, T. Jeans and T. McLaughlin, "Deep Ocean Wave Energy Conversion using a Cycloidal Turbine," *Applied Ocean Research*, vol. Volume 33 Issue 2, pp. 110-119, 2011.
- [14] T. Jeans, C. Fagley, S. G. Siegel and J. Seidel, "Irregular Deep Ocean Wave Energy Conversion Using a Cycloidal Wave Energy Converter," *International Journal of Marine Energy*, vol. 1, pp. 16-32, 2013.
- [15] S. G. Siegel, C. Fagley and S. Nowlin, "Experimental wave termination in a 2D wave tunnel using a cycloidal wave energy converter," *Applied Ocean Research*, vol. 38, pp. 92-99, 10 2012.
- [16] C. Fagley, S. Siegel, J. Seidel, 3d efficiency analysis of cycloidal wave energy converters in oblique wave fields, in: 32nd International Conference on Ocean, Offshore and Arctic Engineering (OMAE). OMAE2013e10876, 2013.
- [17] S.G. Siegel, C. Fagley, J. Seidel, 3d wave diffraction efficiency of a double cycloidal wave energy converter, in: 10th European Wave and Tidal Energy Conference (EWTEC), Aalborg, DK, September 5th-9th, 2013.
- [18] S.G. Siegel, Wave climate scatter performance of a cycloidal wave energy converter, *Appl. Ocean Res.* 48 (2014) 331e343. <https://doi.org/10.1016/j.apor.2014.10.008>.
- [19] S. K. Chakrabarti, *Offshore structure modeling*, World Scientific, 1994.
- [20] F. J. M. Farley, "Capture width for arrays of wave energy converters," in IWWWFB28, 2012.
- [21] J. N. Newman, "The interaction of stationary vessels with regular waves," in *Proc. Symp. Naval Hydrodyn 11th*, 1976.
- [22] R. Yemm, D. Pizer, C. Retzler and R. Henderson, "Pelamis: experience from concept to connection," *Phil. Trans. R. Soc. A*, vol. 370, p. 365-380, 2012.
- [23] J. Falnes, "A review of wave-energy extraction," *Marine Structures*, vol. 20, p. 185-201, 2007.
- [24] S. G. Siegel, "Numerical benchmarking study of a Cycloidal Wave Energy Converter," *Renewable Energy*, vol. 134, pp. 390-405, 2019.
- [25] C. Fagley, A. Mohtat, K. C. Chitale and S. G. Siegel, "Dynamic Estimation and Control of a Cycloidal Wave Energy Converter in Three-Dimensional Sea States," *The European Wave and Tidal Energy Conference*, Plymouth, UK, September 2021
- [26] S. G. Siegel, "Scalability limits of ocean wave energy converters," *International Conference on Ocean Energy (ICOE)*, April 2021.
- [27] K. C. Chitale, C. Fagley, A. Mohtat, and S. G. Siegel, "Numerical Evaluation of Climate Scatter Performance of a Cycloidal Wave Energy Converter," *The European Wave and Tidal Energy Conference*, Plymouth, UK, September 2021.